Fractional proliferation: a method to deconvolve cell population dynamics from single-cell data

Darren R Tyson, Shawn P Garbett, Peter L Frick & Vito Quaranta

We present an integrated method that uses extended time-lapse automated imaging to quantify the dynamics of cell proliferation. Cell counts are fit with a quiescence-growth model that estimates rates of cell division, entry into quiescence and death. The model is constrained with rates extracted experimentally from the behavior of tracked single cells over time. We visualize the output of the analysis in fractional proliferation graphs, which deconvolve dynamic proliferative responses to perturbations into the relative contributions of dividing, quiescent (nondividing) and dead cells. The method reveals that the response of 'oncogene-addicted' human cancer cells to tyrosine kinase inhibitors is a composite of altered rates of division, death and entry into quiescence, a finding that challenges the notion that such cells simply die in response to oncogene-targeted therapy.

Proliferation is a fundamental property of living cells. Altering or controlling cell proliferation—often with chemical compounds—is a major goal of several disciplines, including oncology, tissue engineering and developmental biology. Many current proliferation assays rely on surrogate measurements of cell number (such as total ATP or DNA content) rather than direct cell counts[1]. Moreover, because cells are not directly visualized in most proliferation assays, their states (dividing, quiescent and apoptotic) are unknown; a given proliferation curve could be the consequence of one of many combinations of states. Proliferation assays are also typically performed with few time points and rarely account for proliferation dynamics. Flow cytometry provides measurements at the single-cell level, which include cell cycle position[2], expression of proliferative markers, fractions of dead or dying cells[3] and division tracking by dye dilution[4]. However, adherent cells must be detached for end-point analysis, and single cells cannot be tracked or individual cell histories recorded.

We describe a methodology to quantify dynamic changes in a proliferating cell population and to deconvolve fractional cell fates over time (**Fig. 1**). We label cells with a nuclear fluorescent protein, carry out extended time-resolved automated microscopy (typically for ~96 h and as long as 10 d), segment nuclei in image stacks to directly count cells, and track single cells to determine cell lifespans and fates (Online Methods). The large image data sets require analysis with computational tools and newly developed mathematical models (**Supplementary Notes 1** and **2**) that utilize information at both the population and single-cell levels and integrate them into a model of cell proliferation dynamics (**Fig. 1**). Briefly, we fit cell count data obtained from time-lapse automated microscopy with a novel quiescence-growth model, which incorporates rates of cell division, entry into quiescence and death. The model is constrained with experimental rates derived from tracked single cells, and its output is visualized in fractional proliferation graphs. These graphs resolve the dynamic change in total cell numbers into fractions of dividing and quiescent cells.

RESULTS

Quiescence-growth model of cell population dynamics

We used our approach to monitor the proliferation dynamics of drug-treated cells. Cell counts extracted from the image data show that vehicle- and cycloheximide (CHX)-treated PC9 cells exhibited linear proliferation (in log scale). In contrast, treatment with erlotinib, lapatinib, PLX-4720 or doxorubicin resulted in nonlinear effects on proliferation of PC9 cells (**Fig. 2a**). We observed similar effects in other cell lines (**Supplementary Fig. 1**). We analyzed the expression of a marker of S or G2 phases (mAG-geminin)[5] in drug-treated cells: erlotinib, lapatinib and PLX-4720 induced arrest in G1 (or G0), and doxorubicin induced arrest in S or G2 (**Fig. 2b**). These results suggest a correlation between cell cycle arrest and nonlinear proliferation. We also observed this correlation in erlotinib-treated PC9 cells analyzed using flow cytometry (**Supplementary Fig. 2a**,**b**) and in MCF10A cells deprived of serum (**Supplementary Fig. 2c**). Nonlinear population dynamics are traditionally modeled using logistic or Gompertz equations[6,7], which have been applied to cultured cells as well as tumors[8–10]. A major assumption of these models is the idea of a 'carrying capacity' representing the maximum size a population can reach in a given environment. There is no clear relationship between carrying capacity and the biological processes that affect cell population size, such as cell division, quiescence and death.

To explain the nonlinear proliferation dynamics using biologically relevant parameters, we constructed a quiescence-growth

Department of Cancer Biology, Vanderbilt University School of Medicine, Nashville, Tennessee, USA. Correspondence should be addressed to D.R.T. (darren.tyson@vanderbilt.edu).

RECEIVED 10 NOVEMBER 2011; ACCEPTED 25 JUNE 2012; PUBLISHED ONLINE 12 AUGUST 2012; DOI:10.1038/NMETH.2138

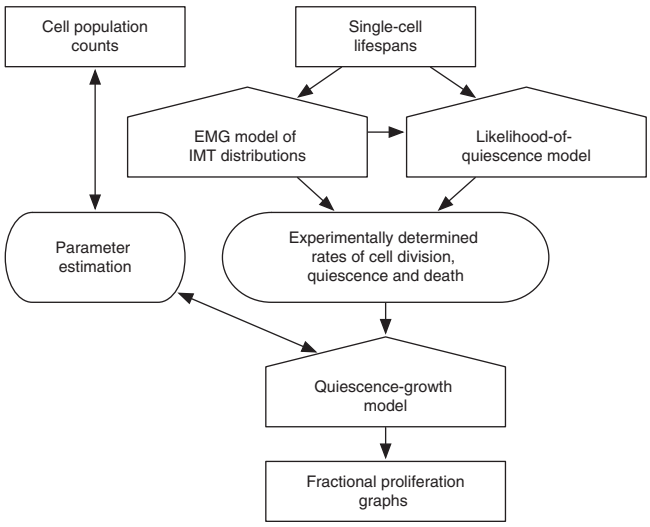

Figure 1 | The fractional proliferation methodology. The principal inputs are cell population counts and metrics of single-cell fate obtained by automated time-lapse imaging. The quiescence-growth model is fit to cell count data to estimate rates of cell division, death and entry into quiescence. These estimated rates are statistically bound and can be evaluated with the quiescence-growth model to provide initial insights into the underlying biology without requiring experimental determination of the rates. The EMG model of IMT distribution and the likelihood-of-quiescence model extract experimental rates of division and entry into quiescence from single-cell tracking data. Incorporating experimentally derived rates constrains the quiescence-growth model and produces fractional proliferation graphs that dynamically resolve the change in cell counts into fractions of dividing and quiescent cells.

model that includes two compartments—a dividing and a non-dividing (which we term quiescent) population—with death occurring in both compartments (**Fig. 2c**, Online Methods and **Supplementary Notes 1** and **2**). The equation derived from this model incorporates three parameters (**Fig. 2c**): rates of division (d), death (a) and entry into quiescence (q). The term 'quiescence' in the quiescence-growth model reflects arrest at any position in the cell cycle. We applied the quiescence-growth model to fit the cell count data obtained from drug-treated PC9 cells (**Fig. 2a**). PC9 response to CHX was linear and is best explained by a drug-induced decrease in the rate of division (d). In contrast, proliferation in response to erlotinib, lapatinib and PLX-4720 was nonlinear and can be explained only by varying the q parameter, the rate of entry into quiescence (**Fig. 2a**). Varying the q parameter also best fits the response to doxorubicin (**Fig. 2a**), which is known to cause arrest in G2 (**Fig. 2b**).

Data-derived quiescence-growth model parameters

Good fits of the cell count data with the quiescence-growth model may be achieved through different combinations of parameter values (**Supplementary Fig. 3**, **Supplementary Table 1** and **Supplementary Software 1**), particularly death and division rates, which oppose each other. We therefore constrained the model with experimentally measured rates from single-cell tracking of time-lapse images.

We first tracked single cells across time-lapse image stacks to quantify observed cell lifespans, which are defined as the time between an initial mitotic event and (i) a death event, (ii) another mitotic event (defining an intermitotic time, IMT), or (iii) the end of the experiment (EoE) (**Fig. 3a**, Online Methods and **Supplementary Video 1**). Cell lifespans demarcated by an initial mitotic event and the EoE may belong to either dividing or nondividing (quiescent) fractions.

For death rates, we identified death events by shrinkage and disintegration of nuclei (**Supplementary Fig. 4a**), tallied these events and converted them directly to rates (Online Methods).

For division rates, we first determined the variability of IMT in the population by examining IMT distributions, which are non-Gaussian by visual inspection (**Fig. 3b**,**c** and **Supplementary Figs. 5** and **6**), fail several statistical tests of normality (**Supplementary Tables 2** and **3**) and cause bias in the estimation of division rate if a simple mean value is used. We searched for model distributions that adequately capture the variability (**Fig. 3b**). Among several possible models we examined (**Supplementary Table 2**), an exponentially modified Gaussian (EMG) model[11] fits the observed IMT distributions from a wide range of cells and conditions (**Fig. 3** and **Supplementary Figs. 5** and **6**) while minimizing the number of parameters to three. An additional benefit is that EMG model parameters are mathematically and biologically separable: that is, their values are differentially affected by drugs (**Supplementary Fig. 6**).

We adapted a method of calculating division rates in bacterial cultures[12] to utilize all EMG parameters fit to the observed IMT distribution (**Supplementary Notes 1** and **2**). This method accounts for the dispersion of individual IMT, especially the

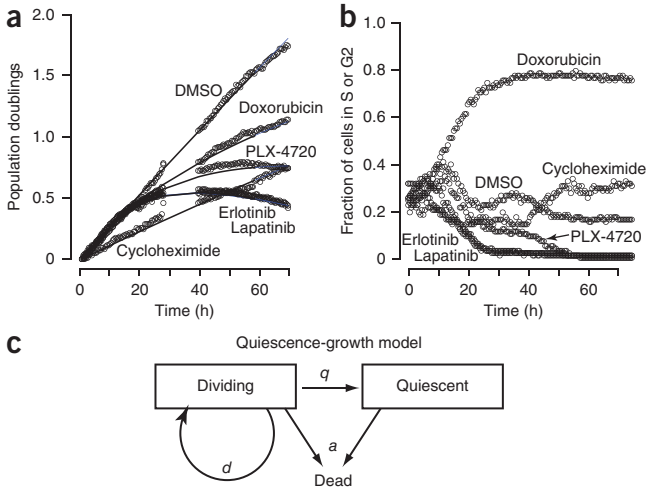

Figure 2 | The quiescence-growth model explains nonlinear proliferation. (**a**) The number of population doublings of PC9 cells treated with the vehicle (DMSO) or the indicated drugs is shown as circles (see Online Methods). Drug concentrations: cycloheximide, 250 ng ml^{-1}; erlotinib, 4 μM; lapatinib, 4 μM; PLX-4720, 16 μM; doxorubicin, 31 nM. The lines indicate quiescence-growth model fits to the data. (**b**) PC9 cells treated as in **a** (except 250 ng ml^{-1} doxorubicin) were analyzed for their expression of a marker of S or G2 phase (mAG-geminin)[5]. After ~15 h the data plotted for erlotinib and lapatinib overlap substantially and are essentially indistinguishable. (**c**) The quiescence-growth model considers two cellular compartments: dividing and nondividing (quiescent). The dividing-cell compartment is depleted at the rate of entry into quiescence (q) and replenished at the rate of division (d). A rate of death (a) depletes both compartments. The differential equations derived from the model are shown in the Online Methods.

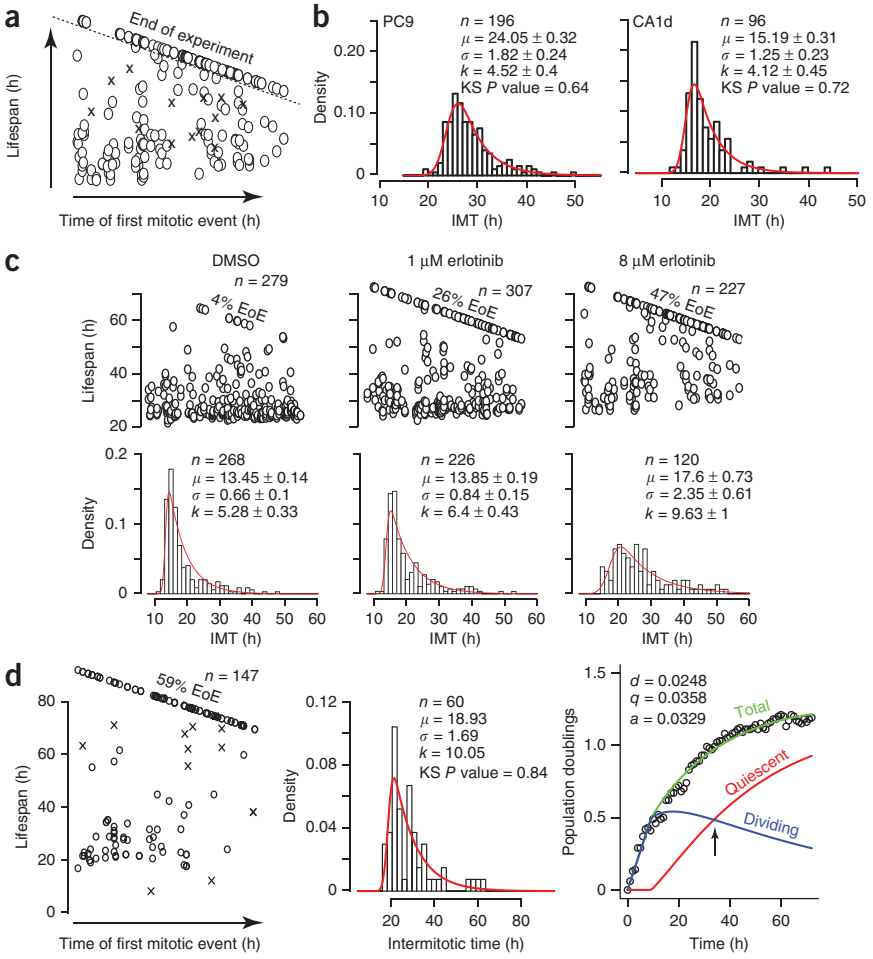

Figure 3 | Interpretation of tracked single-cell data with mathematical models. (**a**) Schematic example plot of tracked single-cell lifespans. The data used in this example plot are shown in **c** (CA1d cells treated with 8 μM erlotinib). Time of first mitotic event (birth time) is along the *x* axis, and cell lifespan is along the *y* axis. O, live cells; X, dead cells. Cells born during the experiment but reaching the end of experiment (EoE) without a second mitotic event are above the dashed line and are not included in IMT distributions. (**b**) Representative IMT distributions of untreated populations of the indicated cell types. Distributions were fit to an EMG model. *n*, number of observed IMTs included in the distribution; μ, mean of the Gaussian component of EMG; σ, deviation of the Gaussian component of EMG; *k*, mean of the exponential component of EMG. μ, σ and *k* are values ± 95% confidence intervals. The *P* value of the Kolmogorov-Smirnoff (KS) test indicates that the EMG model cannot be excluded as an explanation for the data ($P > 0.05$). (**c**) Plots of single-cell lifespans (top) and IMT distributions (bottom) of CA1d cells treated with indicated concentrations of erlotinib or vehicle (DMSO). (**d**) Plots showing proliferation of CA1d cells treated with 16 μM erlotinib. Single-cell lifespans (left), the IMT distribution (middle) and the fractional proliferation graph (right) are shown. The fractional proliferation graph (Online Methods) shows total cells (green) and the fractions of dividing (blue) and nondividing cells (red) over time. The arrow indicates the time at which quiescent and dividing fractions are equal. Note that the death rate is not explicitly represented but is applied to both quiescent and dividing fractions.

slowly dividing cells in rightward-skewed tails. In addition, this calculation of the division rate takes into account the age structure of an asynchronously dividing cell population under the assumption of exponential growth.

For quiescence rates, a crucial question is whether cells with lifespans demarcated by an initial mitotic event and the EoE are quiescent or whether they would have divided if the experiment had continued (**Fig. 3a**). We estimated the probability that a cell is quiescent by implementing a likelihood-of-quiescence model based on a statistical survival formula[13] (Online Methods and **Supplementary Notes 1** and **2**). The older the undivided cell relative to the distribution, the lower the likelihood that it would have divided after the EoE and the higher the likelihood that it would have been quiescent. The rate of entry into quiescence was then calculated using the fraction of quiescent cells in the population and is relative to the calculated rate of division. Notably, without properly accounting for the slowly dividing cells in the population with a well-fit model (such as an EMG), the rate of entry into quiescence could be significantly overestimated.

We experimentally derived the three quiescence-growth model parameters from single-cell tracking data of CA1d cells (**Fig. 3c**) treated with erlotinib (1 and 8 μM). Compared to the control (dimethylsulfoxide (DMSO)-treated) cells, more erlotinib-treated cells reached the EoE without dividing and were estimated to be quiescent by the likelihood-of-quiescence model (**Table 1**). The IMT distribution of cells treated with 8 μM erlotinib was flattened and elongated rightward (**Fig. 3c**). Rates calculated from the single-cell tracking data, EMG parameters and estimated quiescence fraction confirmed a decreased rate of division, a slight increase in death rate and a tenfold increase in the rate of entry into quiescence at either erlotinib concentration. These experimentally measured rates were in agreement with the rates estimated from fitting the quiescence-growth model to the cell count data (**Supplementary Fig. 3** and **Supplementary Table 1**), thus indicating that the quiescence-growth model provides an accurate description of cell proliferation and validating its prediction that the nonlinear proliferation response to erlotinib (**Fig. 2a**) is explained by altering the rate of entry into quiescence (**Fig. 3c**). We observed that few cells died during

Table 1 | Quiescence-growth model parameters obtained from single-cell tracking data

	DMSO	1 μM erlotinib	8 μM erlotinib
f_{EoE}	0.04	0.26	0.47
f_Q	0.04	0.26	0.41
d	0.0379	0.035	0.0241
DT_d	18.3 h	19.8 h	28.8 h
q	0.0015	0.0123	0.0167
a	0.0012	0.0013	0.0018

The following parameter values were calculated from the data shown in **Figure 3c**: fraction of live cells reaching the end of experiment, f_{EoE}; fraction of quiescent cells, f_Q; division rate, *d*; doubling time of dividing cells only, DT_d; and rate of entry into quiescence, *q*. The death rate (*a*) was obtained directly from analyzed image stacks. Values for *d*, *q* and *a* are in h^{-1}.

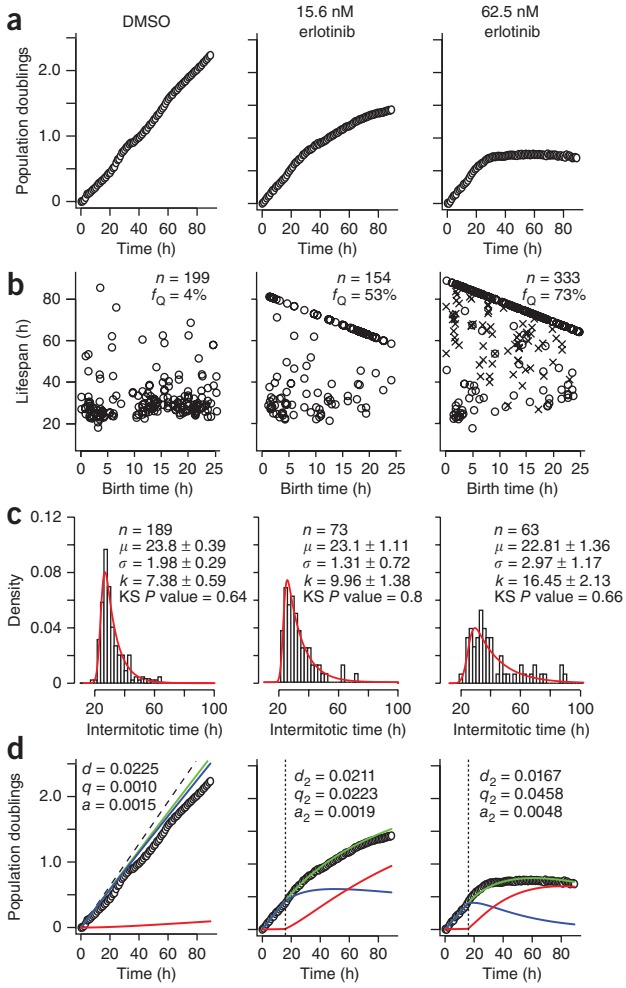

Figure 4 | Application of fractional proliferation to a model of oncogene-addicted tumor cells. (**a**) Plots showing PC9 cell counts obtained by automated quantification of cell nuclei from time-lapse images of cultures treated as indicated. Data were normalized and plotted (open circles) on a $\log_2$ scale (population doublings). (**b**) Lifespan plots of tracked PC9 cells treated as indicated; observed birth time is on the *x* axis and observed lifespan on the *y* axis. Only cells born in the first 25 h of the experiment are shown. f_0, quiescent fraction; *n*, number of lifespans examined. (**c**) IMT distributions of PC9 cells treated as indicated. The EMG model was fit with the parameters shown within each graph. Parameters and KS *P* value as in **Figure 3**. (**d**) Fractional proliferation graphs of erlotinib-treated PC9 cells as in **Figure 3d**. The dashed line (left panel) indicates calculated proliferation without the contribution of death and quiescence (based on the doubling time of dividing cells, DT_d; see **Fig. 3c**). Parameter values (d_2, q_2, a_2) fitting these data are indicated in the boxes and were applied after a delay (vertical dotted line) to account for lag time in drug action.

the experiment, and cells considered quiescent did not exhibit preapoptotic nuclear condensation (data not shown).

Fractional proliferation graphs

We then used the parameters obtained from single-cell tracking data (**Supplementary Video 2**) in the quiescence-growth model to produce graphs of the total population deconvolved into fractions of dividing and quiescent cells (**Fig. 3d** and **Supplementary Software 2**). At ~24 h the fractions of cells in the two compartments were equal (**Fig. 3d**); in contrast, at 80 h the quiescent fraction was 82% and the dividing fraction was 18%.

Drug response of oncogene-addicted cells

We applied this approach to investigate the dynamic response of PC9 cells to erlotinib (**Fig. 4** and **Supplementary Fig. 1c**). PC9 cells harbor activating mutations of the epidermal growth factor receptor (EGFR) and are 'oncogene-addicted'[14] and hypersensitive (that is, concentration of drug required to cause a 50% decrease in cell number (GI50) <20 nM) to EGFR tyrosine kinase inhibitors (TKIs). These cells are representative of EGFR-mutated tumor cells in lung cancer patients that respond favorably to treatment with erlotinib (or other EGFR-specific TKIs). The prevalent view is that PC9 cells have a strong apoptotic response to EGFR TKI[15,16], but, to our knowledge, the relative contributions of cell death versus quiescence in the PC9 response to erlotinib remain uncharacterized.

From cell count data derived from image stacks, PC9 cells exhibited exponential proliferation with a rate = 0.0183 h^{-1} (doubling time = 38 h) in medium containing the vehicle (DMSO); however, single-cell tracking data show that this value underestimates the rate of division and does not consider the contribution of quiescence and death (**Fig. 4d**). Proliferation decreased in a nonlinear fashion upon erlotinib treatment (**Fig. 4a**), and cells accumulated at the EoE (**Figs. 3a** and **4b**). From single-cell tracking data, 53% and 73% of cells with initial mitotic events within the first 25 h entered quiescence in response to 15.6 nM and 62.5 nM erlotinib, respectively, compared to 4% in the control cells. The IMT distributions showed a rightward skew in response to erlotinib characterized by an increased *k* parameter value, whereas all other parameter values remain essentially unchanged (**Fig. 4c**). We calculated the rates of division, death and entry into quiescence from the single-cell tracking data and produced fractional proliferation graphs (**Fig. 4d**). As for CA1d cells, using these rates in the quiescence-growth model correctly predicted the experimentally determined cell counts (**Fig. 4d**). The rate of cell death was 0.0015 h^{-1} in DMSO and increased to 0.0048 h^{-1} in 62.5 nM erlotinib, but this higher death rate cannot by itself explain the decreased proliferation in response to erlotinib. The *q* parameter for 62.5 nM erlotinib-treated cells increased >40-fold over that of DMSO-treated cells (**Fig. 4d**). These results indicate that in oncogene-addicted PC9 cells, the antiproliferative response to erlotinib is primarily due to increased entry into a nondividing or quiescent state, and not to apoptosis as is commonly assumed.

We verified that erlotinib treatment increased the fraction of quiescent PC9 cells by flow cytometry on Ki-67– (**Supplementary Fig. 7**) and p27–immunostained cells (not shown). We confirmed these observations in another oncogene-addicted model cell line (A375, representing BRAF V600E–mutated melanoma) (**Supplementary Note 3** and **Supplementary Figs. 7** and **8**). The nondividing quiescent state we observed was not equivalent to a preapoptotic state; after 96 h in 1 μM erlotinib, a drug washout experiment showed that proliferation resumed to pretreatment levels (**Supplementary Video 1** and **Supplementary Fig. 9**). Also, a large fraction of cells remained viable (Ki-67 positive) after more than 90 h of erlotinib treatment (**Supplementary Fig. 7**). Determining the eventual fate of these cells (division, death or extended quiescence) would require studies of longer duration.

Application to primary cells

We assessed the performance of our approach on primary cells using baculovirus-based transduction of a genetically encoded fluorescent nuclear probe that is easy to use and commercially available (CellLight Nucleus, Invitrogen). Labeled nuclei were detectable within 12 h, persisted for 5–6 d, and were amenable to automated counting and manual tracking. As an example, the proliferation of primary human squamous cell carcinoma cells is shown in **Supplementary Figure 10** and **Supplementary Video 3**. It is worth noting that an EMG distribution also describes the distribution of IMT in primary cultured cells. Additional experimentation will be required to determine whether this distribution is applicable to all cell types.

DISCUSSION

The fractional proliferation method provides quantitative insight into cell proliferation in response to perturbations and permits deconvolution of the relative contribution of multiple cell fates to cell population dynamics. Using this approach, it is possible to capture the behavior of minor subpopulations of cells (for example, stem or progenitor cells, clonal variants and drug-resistant phenotypes) within perturbed populations. The importance of these subpopulations is increasingly appreciated, and methods to study them should be broadly applicable.

The integrated mathematical models we developed describe the emergence of population behavior from experimental data measuring single-cell fates. We note that these models are not definitive—for example, they will need to be adjusted to more accurately accommodate age structure in asynchronously dividing populations; to apply them to stem cells, a rate of entry into one or more differentiated states would have to be included. However, image data sets such as those described here can be analyzed by future models. Furthermore, the approach could be enhanced by the incorporation of other readouts, such as immunofluorescence of molecular markers or live-cell reporters of molecular activity.

Time-lapse video microscopy has been used for decades, but its high-throughput implementation has only recently been enabled by technological advances in automated microscopy instrumentation coupled to computation. Methods to automate the extraction of mitotic phases and duration from time-lapse movies were recently developed[17–19]. These approaches focus mainly on extracting image features that correlate with mitotic events.

The labeling approach we employed involves the expression of a fluorescent nuclear protein (H2BmRFP) introduced by recombinant viral particles. Although other labeling techniques are feasible, and even phase-contrast imaging can provide data amenable to this approach, the use of H2BmRFP overcomes limitations due to photobleaching, toxicity, low signal-to-noise ratio in images and fluctuating subcellular localization. In our experience, nuclear dyes (such as Hoechst 33342) demonstrate significant toxicity, and cytoplasmic and membrane dyes (such as carboxyfluorescein diacetate succinimidyl ester and carbocyanine-based dyes) are prone to photobleaching, tend to aggregate in vesicles and pose challenges to identification of individual cells. The development of nontoxic fluorescent nuclear dyes would enable rapid cell labeling without genetic manipulation.

Observation of cells for several days permits study of the cell response to perturbations as they approach population steady state, which usually happens over many days of treatment. Our discovery that entry into a quiescent state is a major component of the PC9 response to TKI erlotinib challenges the current view that the predominant response to erlotinib in oncogene-addicted cells is cell death[16], but it is consistent with previous reports that erlotinib and other EGFR TKIs induce cell cycle arrest in G1 in many cancer cell lines[20–22].

Erlotinib is of special interest because it is currently used clinically as an adjuvant or first-line therapy in subsets of lung cancer patients with sensitizing EGFR mutations (for reviews on the subject, see refs. 23,24). Questions remain as to the basis of oncogene addiction in EGFR-mutated cancer cells and the inevitable rise of resistance to EGFR-targeted therapy[25]. As we have demonstrated, application of the fractional proliferation method should help answer these questions.

Describing IMT distributions with an EMG model provides value beyond calculating the rates of division and quiescence in the quiescence-growth model. The EMG model is mathematically separable into two components: exponential and Gaussian. Intriguingly, erlotinib primarily affects the exponential (k), whereas CHX primarily affects the mean of the Gaussian (μ) (**Supplementary Fig. 6**). The possibility that these separable components reflect distinct biochemical mechanisms is currently under investigation. The EMG can be interpreted biologically as a combination of a Gaussian process (several random variables that are additive, such as protein accumulation) and an exponential process (for example, a checkpoint process such as the G1-S transition, with a chance of passing at each check). Other descriptive distributions offer no simple interpretation biologically[26]. The EMG may be more common in time-dependent cellular processes because of the mathematical properties of the chemical master equation, which can have an exponential distribution of halting times after sufficient time has passed to achieve a well-mixed system[27,28].

It has long been known that antiproliferative responses are not limited to a single fate, but the lack of methods to deconvolve behaviors has forced assumptions of linearity. The fractional proliferation method provides a means to accommodate nonlinear antiproliferative responses and to separate the underlying cellular fates that shape the population-level response.

METHODS

Methods and any associated references are available in the online version of the paper.

Note: Supplementary information is available in the online version of the paper.

ACKNOWLEDGMENTS

We would like to thank J. Hao and A. Udyavar for technical assistance, E. Pham and R. Feroze for assistance in manual image analysis, G. Ostheimer for assistance with flow cytometry and A. Weaver, G. Webb, B. Rexer, K. Dahlman, W. Yarbrough and L. Estrada for reviewing the manuscript and providing stimulating discussions. We acknowledge the generous gift of primary squamous cell carcinoma and SQ20B cells from W. Yarbrough and PC9 cells from W. Pao (both at Vanderbilt University School of Medicine). We also acknowledge A. Miyawaki (RIKEN Brain Science Institute) for the mAG-geminin plasmid and Gideon Bollag (Plexxikon) for the generous gift of PLX-4720. This work was supported by the US National Institutes of Health/National Cancer Institute Integrative Cancer Biology Program (5U54 CA113007-07). Flow cytometry experiments were performed in the Vanderbilt Medical Center Flow Cytometry Shared Resource, which is supported by the Vanderbilt Ingram Cancer Center (P30 CA68485) and the Vanderbilt Digestive Disease Research Center (DK058404). In addition, the project described was partially supported by the National Center for Research Resources (UL1 RR024975-01) and is now at the National Center for Advancing Translational Sciences (2 UL1 TR000445-06).

AUTHOR CONTRIBUTIONS
D.R.T. conceived of the approach, D.R.T. and P.L.F. cultured, treated and imaged cells, D.R.T. analyzed images, S.P.G. and D.R.T. developed the mathematical models, D.R.T. and S.P.G. fit model parameters to data, and D.R.T. and V.Q. cowrote the paper.

COMPETING FINANCIAL INTERESTS
The authors declare no competing financial interests.

Published online at http://www.nature.com/doifinder/10.1038/nmeth.2138. Reprints and permissions information is available online at http://www.nature.com/reprints/index.html.

1. Hughes, M. *et al.* Early drug discovery and development guidelines: for academic researchers, collaborators, and start-up companies. in *Assay Guidance Manual* (eds. Sittampalam, G.S. *et al.*) ⟨http://www.ncbi.nlm.nih.gov/books/NBK92015/⟩ (Eli Lilly & Co. and the National Center for Advancing Translational Sciences, 2004).
2. Terry, N.H. & White, R.A. Flow cytometry after bromodeoxyuridine labeling to measure S and G2+M phase durations plus doubling times *in vitro* and *in vivo*. *Nat. Protoc.* **1**, 859–869 (2006).
3. van Genderen, H. *et al. In vitro* measurement of cell death with the annexin A5 affinity assay. *Nat. Protoc.* **1**, 363–367 (2006).
4. Hawkins, E.D. *et al.* Measuring lymphocyte proliferation, survival and differentiation using CFSE time-series data. *Nat. Protoc.* **2**, 2057–2067 (2007).
5. Sakaue-Sawano, A. *et al.* Visualizing spatiotemporal dynamics of multicellular cell-cycle progression. *Cell* **132**, 487–498 (2008).
6. d'Onofrio, A., Fasano, A. & Monechi, B. A generalization of Gompertz law compatible with the Gyllenberg-Webb theory for tumour growth. *Math. Biosci.* **230**, 45–54 (2011).
7. Gyllenberg, M. & Webb, G.F. Age-size structure in populations with quiescence. *Math. Biosci.* **86**, 67–95 (1987).
8. Florian, J.A. Jr., Eiseman, J.L. & Parker, R.S. Accounting for quiescent cells in tumour growth and cancer treatment. *Syst. Biol. (Stevenage)* **152**, 185–192 (2005).
9. Kozusko, F. & Bajzer, Z. Combining Gompertzian growth and cell population dynamics. *Math. Biosci.* **185**, 153–167 (2003).
10. Turner, M.E. Jr., Bradley, E.L. Jr., Kirk, K.A. & Pruitt, K.M. A theory of growth. *Math. Biosci.* **29**, 367–373 (1976).
11. Grushka, E. Characterization of exponentially modified Gaussian peaks in chromatography. *Anal. Chem.* **44**, 1733–1738 (1972).
12. Powell, E.O. Growth rate and generation time of bacteria, with special reference to continuous culture. *J. Gen. Microbiol.* **15**, 492–511 (1956).
13. McLachlan, G.J. & Peel, D. *Finite Mixture Models* (Wiley, 2000).
14. Weinstein, I.B. & Joe, A.K. Mechanisms of disease: oncogene addiction—a rationale for molecular targeting in cancer therapy. *Nat. Clin. Pract. Oncol.* **3**, 448–457 (2006).
15. Gong, Y. *et al.* Induction of BIM is essential for apoptosis triggered by EGFR kinase inhibitors in mutant EGFR-dependent lung adenocarcinomas. *PLoS Med.* **4**, e294 (2007).
16. Sharma, S.V. *et al.* A chromatin-mediated reversible drug-tolerant state in cancer cell subpopulations. *Cell* **141**, 69–80 (2010).
17. Harder, N. *et al.* Automatic analysis of dividing cells in live cell movies to detect mitotic delays and correlate phenotypes in time. *Genome Res.* **19**, 2113–2124 (2009).
18. Held, M. *et al.* CellCognition: time-resolved phenotype annotation in high-throughput live cell imaging. *Nat. Methods* **7**, 747–754 (2010).
19. Sigoillot, F.D. *et al.* A time-series method for automated measurement of changes in mitotic and interphase duration from time-lapse movies. *PLoS ONE* **6**, e25511 (2011).
20. Bos, M. *et al.* PD153035, a tyrosine kinase inhibitor, prevents epidermal growth factor receptor activation and inhibits growth of cancer cells in a receptor number-dependent manner. *Clin. Cancer Res.* **3**, 2099–2106 (1997).
21. Ciardiello, F. & Tortora, G. A novel approach in the treatment of cancer: targeting the epidermal growth factor receptor. *Clin. Cancer Res.* **7**, 2958–2970 (2001).
22. Ling, Y.H. *et al.* Erlotinib, an effective epidermal growth factor receptor tyrosine kinase inhibitor, induces p27KIP1 up-regulation and nuclear translocation in association with cell growth inhibition and G1/S phase arrest in human non-small-cell lung cancer cell lines. *Mol. Pharmacol.* **72**, 248–258 (2007).
23. Grünwald, V. & Hidalgo, M. Developing inhibitors of the epidermal growth factor receptor for cancer treatment. *J. Natl. Cancer Inst.* **95**, 851–867 (2003).
24. Pao, W. & Chmielecki, J. Rational, biologically based treatment of EGFR-mutant non-small-cell lung cancer. *Nat. Rev. Cancer* **10**, 760–774 (2010).
25. Riely, G.J. *et al.* Clinical course of patients with non-small cell lung cancer and epidermal growth factor receptor exon 19 and exon 21 mutations treated with gefitinib or erlotinib. *Clin. Cancer Res.* **12**, 839–844 (2006).
26. Golubev, A. Exponentially modified Gaussian (EMG) relevance to distributions related to cell proliferation and differentiation. *J. Theor. Biol.* **262**, 257–266 (2010).
27. Sbano, L. & Kirkilionis, M. Multiscale analysis of reaction networks. *Theory Biosci.* **127**, 107–123 (2008).
28. Chichagov, V.V. Asymptotic behavior of the first arrival time in Markovian random walks. *J. Math. Sci.* **39**, 2944–2948 (1987).

ONLINE METHODS

Software. We provide (i) an interactive Mathematica CDF Player file to explore the effects of altering quiescence-growth model parameter values on cell proliferation plots (**Supplementary Software 1**), (ii) an ImageJ[29,30] macro for automated cell counting (enumeration of nuclei) (**Supplementary Note 2**), and (iii) fracprolif, an extension of the freely available statistical software package R[31] (http://www.r-project.org/) that incorporates all of the code (**Supplementary Software 2**) used to analyze single-cell tracking and cell count proliferation data and generate fractional proliferation graphs (described in **Supplementary Note 2**).

Cell culture and labeling. The following cell lines were used: MCF10A, MCF10A-CA1d (abbreviated as CA1d), SQ20B and PC9. MCF10A and CA1d cells were cultured in DMEM/F12 medium containing 10% equine serum, 5% FBS, 20 ng/ml epidermal growth factor, 10 μg/ml insulin, 500 ng/ml hydrocortisone and 100 ng/ml cholera toxin. SQ20B cells were cultured in DMEM containing 20% FBS and 400 ng/ml hydrocortisone, and PC9 cells were cultured in RPMI 1640 medium containing 10% FBS. Primary human tumor-derived cells were obtained from a patient with squamous cell carcinoma of the tongue and were grown continuously in culture in keratinocyte (serum-free) growth medium (Invitrogen). Cell lines were engineered to express the histone H2B–monomeric red fluorescent protein (H2B-mRFP) fusion protein using lentivirus-mediated transduction as previously described[32]. Brightly fluorescent single-cell clones were expanded and compared to parental populations using traditional proliferation measurements to ensure they were representative of the initial population. Primary cells were induced to express H2B-mRFP using recombinant baculoviral particles (CellLight Nucleus, Invitrogen) at 20 particles per cell according to the manufacturer's instructions.

Imaging with extended temporally resolved automated microscopy (ETRAM). Imaging was performed on 96-well plates (BD cat. no. 353219) using a BD Pathway 855 with a 20× (0.75 NA) objective in a CO_2- and temperature-controlled environment. Images were acquired every 6–30 min using BD Attovision 1.6.2 software with the instrument in confocal mode (spinning disk). Nine adjacent images were captured at 0.4-s exposure and 2 × 2 binning to comprise a single 3 × 3 montage (approximately 800 μm^2) from each of approximately 40–60 wells per experiment, and images were acquired for at least 72 h. Example montaged images are shown in **Supplementary Figure 1a**. Assays minimally included duplicate or triplicate wells, and complete experiments were performed at least twice. Cells were seeded at 2,500–5,000 cells per well and were allowed to grow overnight, which yielded approximately 200–600 cells at the onset of imaging. Cells were imaged until confluence (approximately 3,000 cells in an image) was achieved in control wells. Erlotinib concentration-response curves on PC9 cells were performed five or more times.

Enumerating nuclei. Nuclei were counted from ETRAM-generated image stacks sampled at approximately 1-h intervals. Images were imported into the freely available ImageJ (http://rsb.info.nih.gov/ij/) program and subjected to a macro optimized for images obtained from a BD Pathway 855. The macro (i) corrects for uneven illumination using a 50-pixel-diameter rolling ball filter, (ii) converts images to binary using a predefined threshold intensity value, (iii) segments individual nuclei using a watershed algorithm, and (iv) quantifies objects within a specified range of areas and circularity. Example images and resultant cell population plots are shown in **Supplementary Figure 1a**,**b**. The ImageJ macro is provided in **Supplementary Note 2**, and an example image sequence showing nuclei enumeration by ImageJ is shown in **Supplementary Figure 4**.

Quantifying rates of cell death. An example of a region of a manually tracked ETRAM-generated image stack is shown in **Supplementary Video 1**. Cell death was identified by nuclear shrinkage to less than 50% of average nuclear area and subsequent nuclear dispersion or detachment (that is, the nucleus was no longer detectable) (**Supplementary Fig. 4**). Rates of cell death were determined by dividing the number of events (cell deaths) detected across all frames by the total cell observation time (the number of cell nuclei in each frame multiplied by the time interval between frames); this rate does not require individual cells to be tracked over complete lifespans.

Quantifying intermitotic times and rate of division. For most cell lines, ETRAM was performed at 12-min intervals to minimize light exposure and phototoxicity, and for highly motile cells, at 6-min intervals to eliminate bias against faster-moving cells.

Intermitotic times were measured by manually tracking individual nuclei through the series of ETRAM-generated images, identifying mitotic events (metaphase chromosomes) and determining the number of frames between mitotic events for each individual cell lifespan. Lifespans of cell nuclei that divided once during the experiment but reached the EoE were also determined. We tracked 100 nuclei for each condition, and more if too many cells reached the EoE without having divided, as a minimum of 50 individual IMTs represented a distribution.

Model of proliferation kinetics (quiescence-growth model). The quiescence-growth model is formulated as a pair of coupled ordinary differential equations in which x represents the dividing cell number, y represents the quiescent cell number, and $x + y$ equals the total cell population. The rates are described by the three parameters: d for division or birth rate, q for quiescence rate and a for death rate.

$$x' = (d - q - a)x$$

$$y' = qx - ay$$

which has an analytical solution of the following form

$$x(t;x_0,d,q,a) = x_0 e^{(d - q - a)t}$$

$$y(t;x_0,y_0,d,q,a) = \left(y_0 + x_0 \frac{q}{d - q}(e^{(d - q)t} - 1) \right) e^{-at}$$

On a log scale the model is nonlinear because of the quiescence compartment (y). Also of note, when $d = q$, the following

solution applies

$$\lim_{d \to q} y(t; x_0, y_0, d, q, a) = e^{-at}(x_0 dt + y_0)$$

When $d \geq (q + a)$, the following asymptotic behavior is observed

$$x + y \sim \frac{d}{d - q} x_0 e^{(d - q - a)t}$$

This shows that the model approaches exponential growth as long as the division rate exceeds the sum of the rates of death and entry into quiescence, and it mathematically proves that the observation of exponential proliferation of a population does not exclude the possibility of quiescence and death. Thus, only in the absence of any death or quiescence does the rate of cell division reflect the rate of proliferation of the population. On the other hand, note that the population could grow exponentially even if nearly half of the cells enter quiescence or die. Furthermore, entry into the quiescent compartment (with rate q) provides the only mechanism by which nonlinear proliferation curves can be achieved. An alternative of the model has been produced in which a different rate of death from each compartment is provided (**Supplementary Note 1**). However, because measuring these different rates from the single-cell data with sufficient statistical power is not yet feasible, the alternative model reverts to the form used in this method.

Statistical methods. To determine whether a model could describe the observed data with sufficient statistical accuracy, a one-sided Kolmogorov-Smirnoff test was performed with a two-sided test being the null hypothesis. This test determines the probability that the data and the model are sampled from the same distribution, and $P < 0.05$ was assumed to be statistically significant evidence that the data and the model represent different distributions.

The Shapiro-Wilk test was used to test for normality. The likelihood of one of two specific models (for example, a linear model compared to the quiescence-growth model) correctly fitting the data was determined using Akaike's information criterion.

29. Abràmoff, M.D., Magalhães, P.J. & Ram, S.J. Image processing with ImageJ. *Biophotonics Int.* **11**, 36–42 (2004).
30. Rasband, W.S. *ImageJ v.1.45p* (US National Institutes of Health, Bethesda, Maryland, 1997–2012).
31. R Development Core Team. *R: A Language and Environment for Statistical Computing* (R Foundation for Statistical Computing, 2010).
32. Quaranta, V. *et al.* Trait variability of cancer cells quantified by high-content automated microscopy of single cells. *Methods Enzymol.* **467**, 23–57 (2009).

doi:10.1038/nmeth.2138